



Article

Analysis of Stator-Slot Circumferentially Magnetized PM Machines with Full-Pitched Windings

Huan Qu, Han Yang and Zi Qiang Zhu *

Department of Electronic and Electrical Engineering, University of Sheffield, Mappin Street, Sheffield S1 3JD, UK; hqu2@sheffield.ac.uk (H.Q.); czyanghan@hotmail.com (H.Y.)

* Correspondence: z.q.zhu@sheffield.ac.uk; Tel.: +44-(0)-114-222-5195

Abstract: Stator-slot circumferentially magnetized PM machines (SSCMPMMs) have high fault-tolerant capability. In this paper, the SSCMPMMs with full-pitched windings and different stator slot/rotor pole numbers are investigated, together with the influence of key geometric parameters. It shows that the 12 stator-slots 7 rotor-poles (12S7R) machine delivers the highest torque. It is then compared with the SSCMPMM with tooth-coil windings. The results show that when they have the same active length, the 12S7R machine delivers significantly higher torque and higher efficiency. Furthermore, when the machine length is over around 140 mm, the 12S7R machine is more advantageous in producing high torque and high efficiency. A prototype is manufactured and tested to validate the theoretical analyses.

Keywords: coil pitch; fault-tolerant; permanent magnet (PM); stator PM



Citation: Qu, H.; Yang, H.; Zhu, Z.Q. Analysis of Stator-Slot Circumferentially Magnetized PM Machines with Full-Pitched Windings. *World Electr. Veh. J.* **2021**, *12*, 33. <https://doi.org/10.3390/wevj12010033>

Received: 20 January 2021
Accepted: 18 February 2021
Published: 23 February 2021

Publisher's Note: MDPI stays neutral with regard to jurisdictional claims in published maps and institutional affiliations.



Copyright: © 2021 by the authors. Licensee MDPI, Basel, Switzerland. This article is an open access article distributed under the terms and conditions of the Creative Commons Attribution (CC BY) license (<https://creativecommons.org/licenses/by/4.0/>).

1. Introduction

Electrical machines with permanent magnets (PMs) mounted in the stator, i.e., stator PM machines, have been attracting interests for the last several decades. The stator PM machines have some inherent advantages over the rotor PM machines, e.g., robust salient pole-rotor structure and easy thermal management for the magnets if the forced liquid cooling is employed.

Much research and development have been done to improve the performance of stator PM machines. The location of PMs results in various stator PM machine topologies. PMs can be mounted in the stator yoke, between the stator teeth, along the stator bore surface, and in the stator slot, known as doubly salient PM machines [1–3], switched-flux PM machines [4–7], flux-reversal PM machines [8–13], and stator-slot PM machines [14,15], respectively.

In doubly salient PM machines, PMs are circumferentially magnetized and located in the stator yoke separated by the interval of number of stator teeth equal to the phase number. Hence, they usually use less number and also amount of PMs but have relatively low torque density, although they may exhibit good torque per PM volume. Switched-flux PM machines have circumferentially magnetized PMs sandwiched between the stator teeth and can enhance the airgap flux density by flux focusing, which is favourable for high torque. However, the overload capability of switched-flux PM machines is deteriorated due to high stator core saturation. The airgap flux density in flux-reversal PM machines with a pair of PMs mounted on stator tooth surface relies on the magnet remanence and thickness, and no flux focusing effect can be utilized. It was found that changing the PM arrangement from NSSN type to NSNS type helps to improve the performance almost at no extra cost [16]. Meanwhile, by employing consequent pole PM structure, the PM utilization and electromagnetic performance are both improved [17].

Stator-slot radially magnetized PM machine cannot produce high torque density due to large magnetic reluctance. This issue can be solved by employing Halbach array PM in the stator slot [15]. The side magnets can help to conduct and enhance magnetic flux.

The PMs in the stator slots can also be magnetized circumferentially, so-called stator-slot circumferentially magnetized PM machines (SSCMPMMs) [14], as shown in Figure 1. In addition to the merits shared by other stator PM machines, they are fault-tolerant in terms of uncontrolled overvoltage generator fault under high speed flux weakening operation due to low induced back electromotive force (EMF) on open circuit [18]. However, the torque density of the SSCMPMMs needs to be improved, especially at a light load condition.

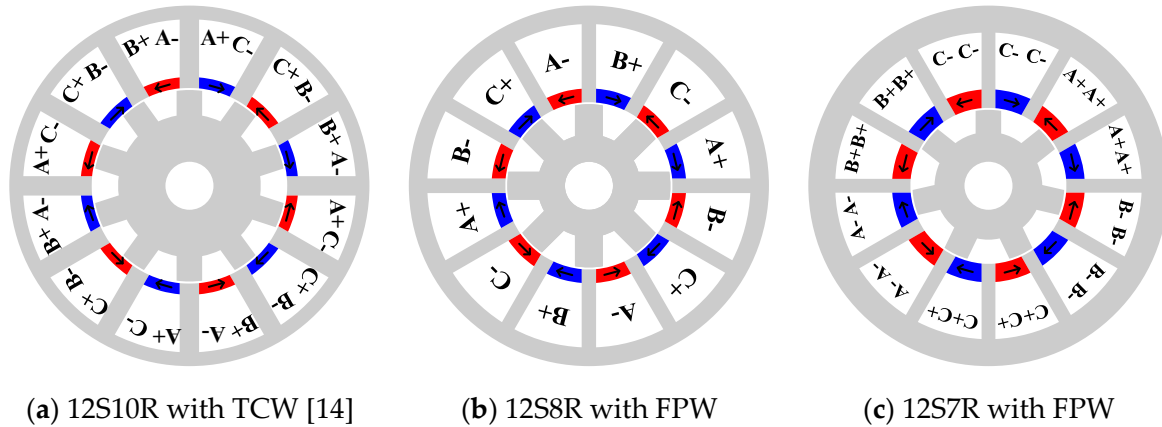


Figure 1. Stator-slot permanent magnet (PM) machines with different winding configurations.

Coil pitch has a significant influence on the torque performance since it affects slot/pole number combination and winding pitch factor. The authors of [19] analytically investigated the influence of coil pitch of 1, 2, and 3 slot pitches on the back EMF of flux-reversal and switched-flux PM machines. It is also found that for both flux-reversal and switched-flux PM machines, distributed windings help to improve torque density compared with tooth-coil windings [20,21]. Therefore, it is necessary to investigate the influence of coil pitch in SSCMPMMs, which is the subject of this paper.

This paper is arranged as follows: Firstly, the machine topology, operation principle, and slot/pole number combinations are introduced in Section 2. The influence of key geometric parameters of SSCMPMMs is investigated in Section 3. The 12 stator-slots 7 rotor-poles (12S7R) machine with full-pitched windings (FPW) is identified to exhibit the highest torque density and then compared with a 12S10R machine with tooth-coil windings (TCW) in Section 4. Finally, a prototype is manufactured and tested in Section 5, and some conclusions are drawn in Section 6.

2. Machine Topology, Operation Principle, and Slot/Pole Number Combination

Figure 1 shows cross sections of stator-slot PM machines. All the machines have circumferentially magnetized magnets in stator slots and two adjacent magnets have opposite magnetization directions. On open circuit, almost all the PM flux is short-circuited within the stator, Figure 2a. However, when the armature windings are excited, the PM flux are forced into airgap and rotor side, Figure 2b. The amount of PM flux forced into airgap and rotor side depends on the armature field strength. Therefore, the average torque under $I_d = 0$ control can be expressed as

$$T = 1.5N_r\psi_{PM}(i_q)i_q \propto N_r\varphi_{PM}(F_q)F_q \quad (1)$$

in which N_r is the rotor-pole number, $\psi_{PM}(i_q)$ is the PM flux linkage and affected by the armature current i_q , and $\varphi_{PM}(F_q)$ is the PM flux and affected by the armature magnetomotive force (MMF) F_q .

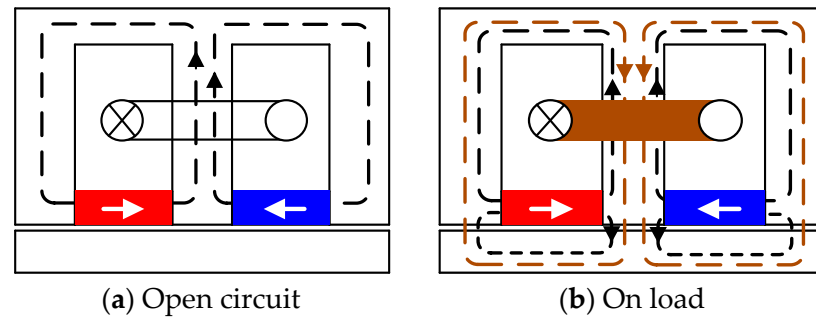


Figure 2. Simplified circuits for illustrating operation principle.

Stator-slot PM machines consist of three parts as other flux modulation machines, i.e., armature, PM excitation (PM MMF), and modulation poles (rotor slots). Although the PM MMF is closely related to the armature MMF, stator-slot PM machines still comply to the principle of flux modulation effect. The pole-pair number of armature windings affects the rotor-pole number, and their relationships are determined by [9]

$$N_r = iN_s/2 \pm P_a \quad (i = 1, 3, 5 \dots) \quad (2)$$

in which N_r is the rotor-pole number, N_s is the stator-slot number, i is the odd number, and P_a is the pole-pair number of armature windings. 12S-4R/8R/10R/11R/13R/14R/16R stator-slot PM machines are mentioned in [14], and the corresponding P_a is 2, 2, 4, 5, 5, 4, and 2, respectively, but all with tooth-coil windings. However, there are other combinations, e.g., 12S-5R/7R, whose armature pole-pair number is 1, as shown in Table 1. In this paper, 12 stator-slots machines with FPW and different number of rotor poles are investigated. The coil pitches are 3, 6, 6, and 3 slot pitches, respectively. It should be noted that FPW is not restricted to 12 stator-slots machines.

Table 1. Different rotor-pole number combinations when $N_s = 12$.

N_r	P_a	$iN_s/2$	Coil Pitch of Full Pitch
4	2	6 ($i = 1$)	3
5	1	6 ($i = 1$)	6
7	1	6 ($i = 1$)	6
8	2	6 ($i = 1$)	3
10	4	6 ($i = 1$)	1
11	5	6 ($i = 1$)	1
13	5	18 ($i = 3$)	1
14	4	18 ($i = 3$)	1
16	2	18 ($i = 3$)	3
17	1	18 ($i = 3$)	6
19	1	18 ($i = 3$)	6
20	2	18 ($i = 3$)	3

Taking 12S7R machine for example, as shown in Figure 3, the coil positions in mechanical degree and electrical degree are shown in Figure 3b,c, respectively. Figure 4 shows the winding layout and back EMF phasors of 12S-4R/5R/7R/8R machines. 12S-5R/7R machines have two sets of balanced three-phase windings that are phase shifted by 30 electrical degrees. For 12S-4R/8R stator rotor-pole machines, there is no shift angle between two sets of windings.

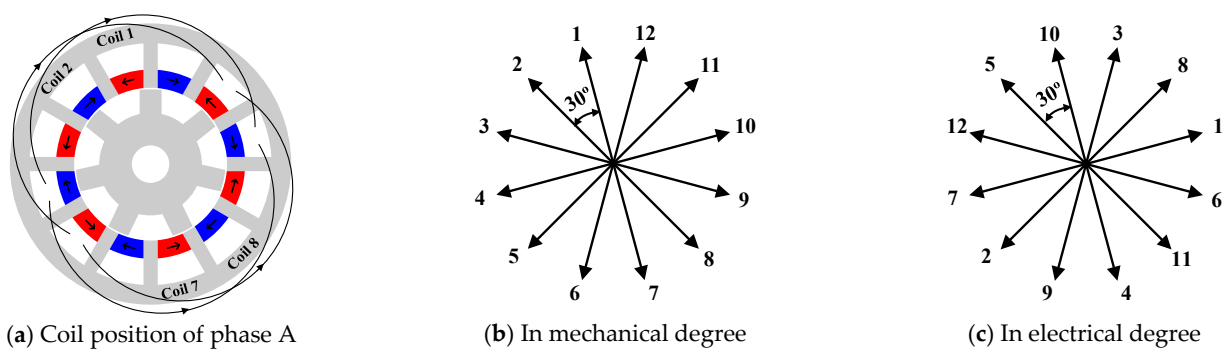


Figure 3. Coil positions of 12S7R stator/rotor-pole machine.

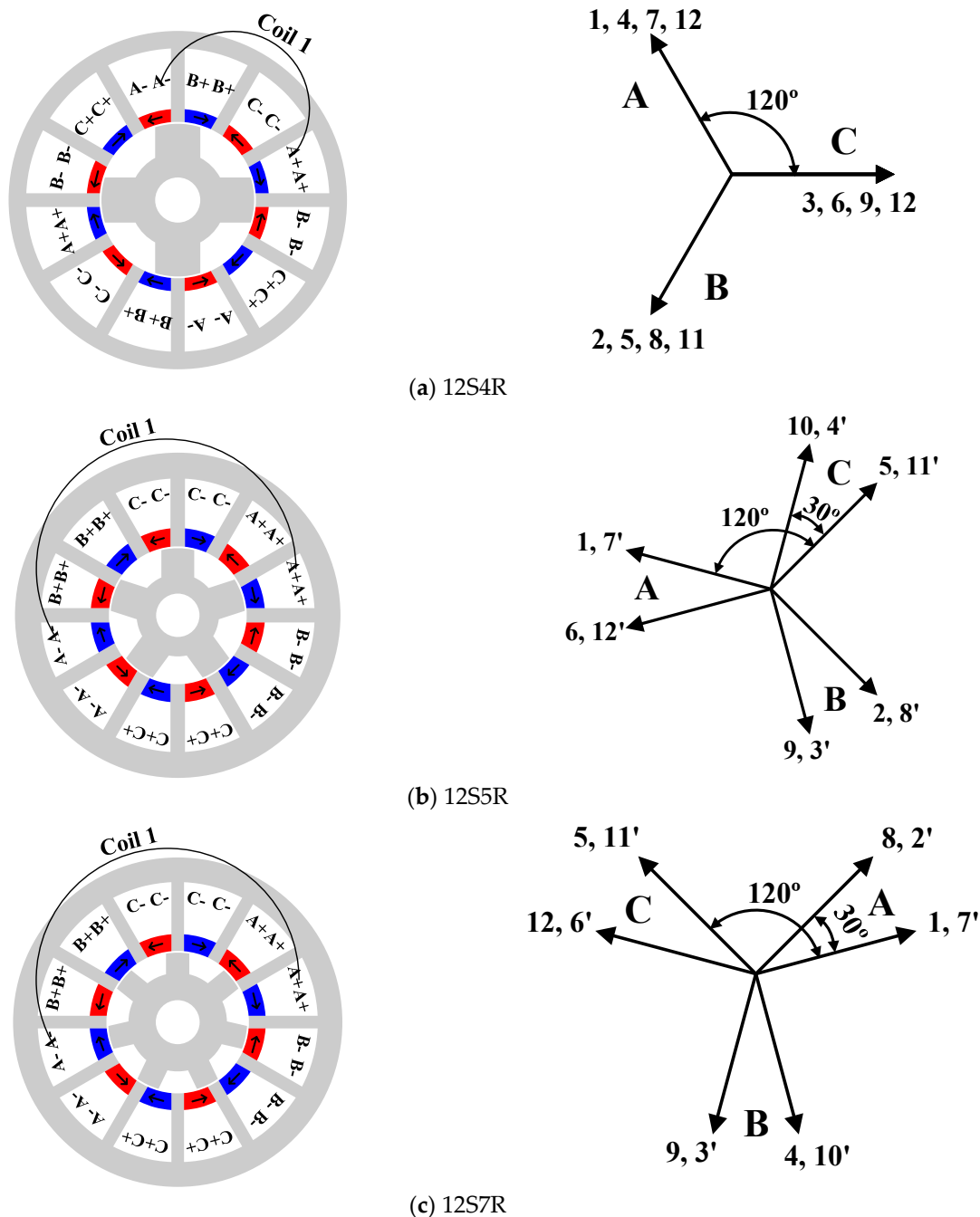


Figure 4. Cont.

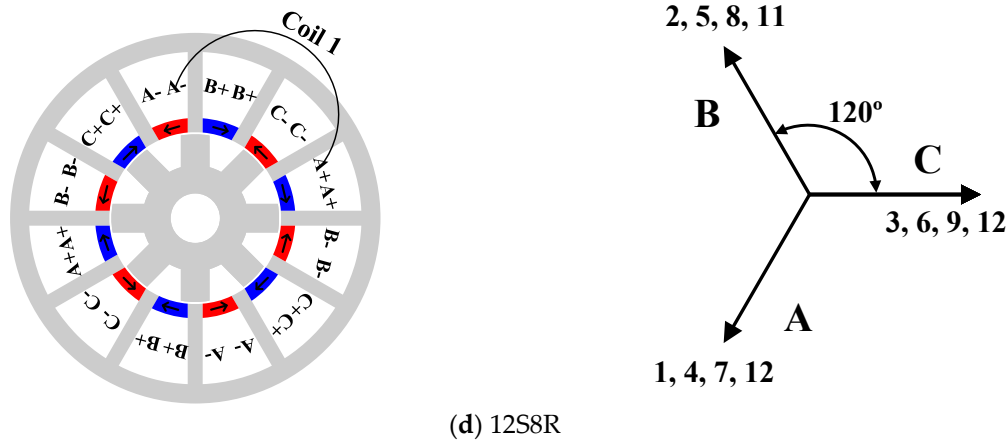


Figure 4. Winding layouts and back electromotive force (EMF) phasors.

The winding factor k_w can be expressed as

$$k_w = k_d k_p \quad (3)$$

where k_d is the winding distribution factor, and k_p is the pitch factor. k_d is given by

$$k_d = \sin(Qv\alpha/2)/(Q \sin(v\alpha/2)) \quad (4)$$

where Q is the number of coil-EMF phasors per phase, α is the angle between two adjacent coil-EMF phasors, and v is the harmonic order.

The pitch factor k_p is given by [16]

$$k_p = \cos(\theta_c/2 - \pi/2) \quad (5)$$

where θ_c is the angular difference between two adjacent slot conductors for the v^{th} harmonics and is expressed as $v(2\pi N_r/N_s)$.

The efficiency can be predicted by considering the total copper loss ($P_{\text{cu_total}}$), iron loss (P_{iron}), PM eddy current loss ($P_{\text{pm_eddy}}$), as

$$\eta = P_{\text{em}}/(P_{\text{em}} + P_{\text{cu_total}} + P_{\text{iron}} + P_{\text{pm_eddy}}) \quad (6)$$

where P_{em} is the output power. The total copper loss includes the effective copper loss $P_{\text{cu_eff}}$ and the end-winding copper loss $P_{\text{cu_end}}$. The end-winding length per turn l_{end} is calculated as

$$l_{\text{end}} = \tau_c \pi \quad (7)$$

where τ_c is the average coil pitch of the machine. For FPW, τ_c is calculated as

$$\tau_c = 2\pi y(r_3 - yk - 0.5h_{\text{slot}})/N_s \quad (8)$$

For TCW, τ_c is calculated as

$$\tau_c = \pi(r_3 - yk - 0.5h_{\text{slot}})/N_s + 0.5tw \quad (9)$$

where r_3 is the stator outer radius, yk is the stator yoke width, h_{slot} is the slot depth, tw is the tooth width, and y is the coil pitch in slot pitch.

3. Influence of Key Geometric Parameters

Before investigating the influence of key geometric parameters, optimal models are obtained by global optimization under the following conditions.

- (1) Both machines have the same stator outer diameter, stack length, PM material, and iron steel. The effective copper loss is fixed to 20 W.
- (2) All the optimizations are based on genetic algorithm (GA), and 30 individuals in each population with 35 generations have been employed.
- (3) The optimized parameters are stator yoke width, stator inner radius, stator tooth width, rotor tooth width, rotor slot depth, and PM thickness. Parameters of the optimized machines are listed in Table 2.

Table 2. Parameters of optimized topologies.

Symbol	12S4R	12S5R	12S7R (M1)	12S8R	12S10R (M2)	12S10R (M3)
Stator outer radius (mm)				45		
Stack length (mm)				25		
Airgap length (mm)				0.5		
Rated speed (rpm)				600		
PM material				N32EZ		
$B_r, \mu_r @ 20\text{ }^\circ\text{C}$				1.13 T, 1.05		
Winding pole pair number	2	1	1	2	4	4
N_{ph}	128	112	120	128	128	120
PM thickness (mm)	3.5	5.0	4.6	3.45	2.75	3.74
Stator inner radius (mm)	20.3	18.6	19.5	20.8	24.4	25.8
Stator tooth width (mm)	3.6	4	3.45	3.64	4.85	4.67
Stator yoke width (mm)	4.6	7.1	6.72	4.66	1.42	2.2
Rotor tooth width (mm)	14	9.1	6.4	7	6.4	7
Rotor slot depth (mm)	7.6	7.2	5.6	7.7	6.2	5.9
Rated current (Arms/Apeak)				10/14.14		

The influence of key geometric parameters, i.e., rotor-pole number, stator yoke width, stator tooth width, stator inner diameter, PM thickness, and rotor tooth width, is investigated. As listed in Table 1, when P_a is fixed, there are different rotor-pole numbers that can satisfy (2). For example, when $P_a = 1$, the rotor-pole number can be chosen as 5, 7, 17, or 19. Figure 5 shows that when the rotor pole number is 5 or 7, higher torque can be generated. Then, the influence of other geometric parameters in 12S-4R/5R/7R/8R machines is further investigated.

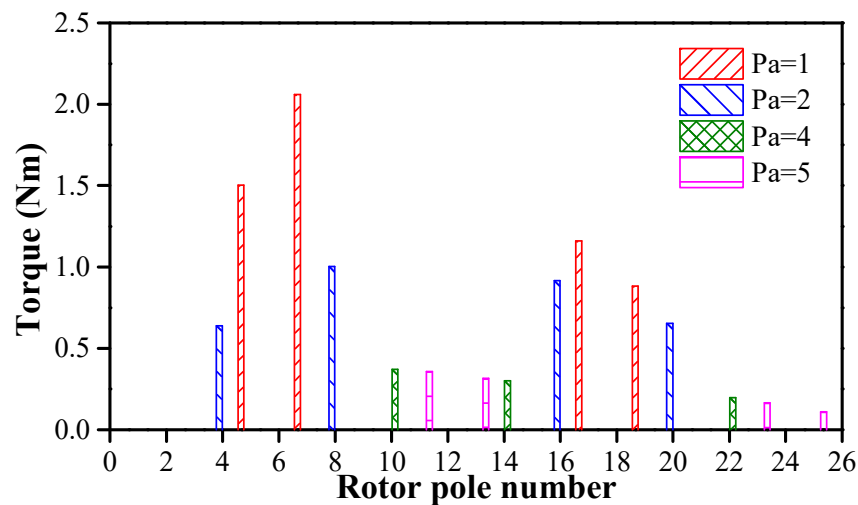


Figure 5. Influence of rotor-pole number on average torque when $P_{cu_eff} = 20$ W.

Figure 6 shows that larger stator yoke width is required to generate the highest torque for 12S5R and 12S7R, because the armature pole pair number is 1 and larger stator yoke

width is required to avoid high saturation. In contrast, 12S4R and 12S8R need smaller optimum stator yoke widths.

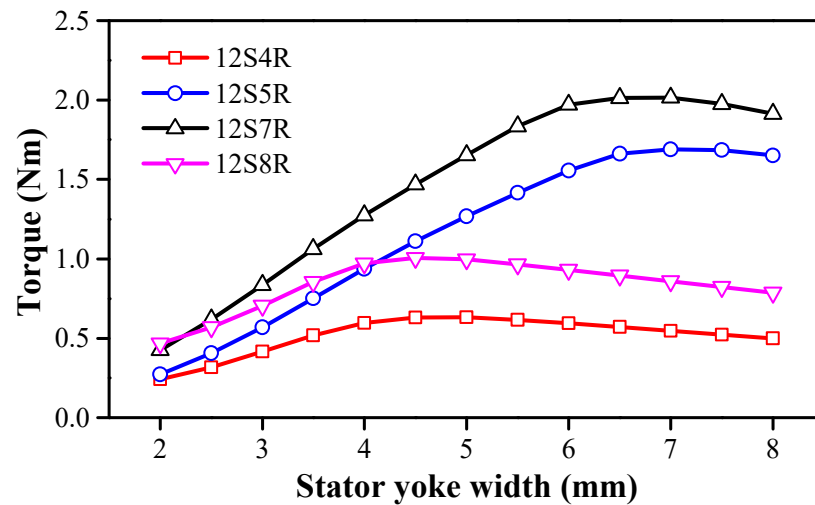


Figure 6. Influence of stator yoke width on average torque when $P_{cu_eff} = 20$ W.

Stator tooth width affects the stator tooth saturation and flux modulation effect. As shown in Figure 7, the optimum stator tooth widths range from 3.5–4.5 mm. Figure 8 shows that there exists an optimum stator inner radius to maximize the average torque, when a better balance is achieved between electrical loading and magnetic loading. For 12S-4R/5R/7R/8R, the optimum values are around 20, 18, 19, and 20 mm, respectively, which correspond to the split ratios between the stator inner radius to outer radius of 0.44, 0.4, 0.42, and 0.44.

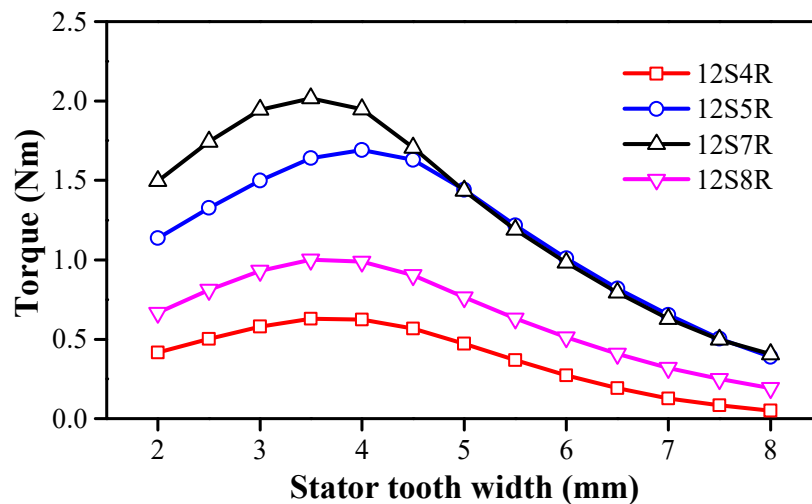


Figure 7. Influence of stator tooth width on average torque when $P_{cu_eff} = 20$ W.

Figure 9 shows that thicker PMs are favourable to produce maximum torque for 12S-5R/7R machines compared to 12S-4R/8R machines. To explain this, the armature MMF of stator windings is analysed. For simplicity, the input current is normalized, and the turn number per slot is 1. Figure 10 compares the MMFs of the two stator windings with $P_a = 1$ and $P_a = 2$. When P_a is smaller, the armature MMF is stronger, and more PM flux can be forced into the airgap and the rotor side under load condition. (1) shows that the average torque is greatly affected by the armature MMF. Hence, the stronger the armature MMF, the higher the PM flux and the thicker the PMs.

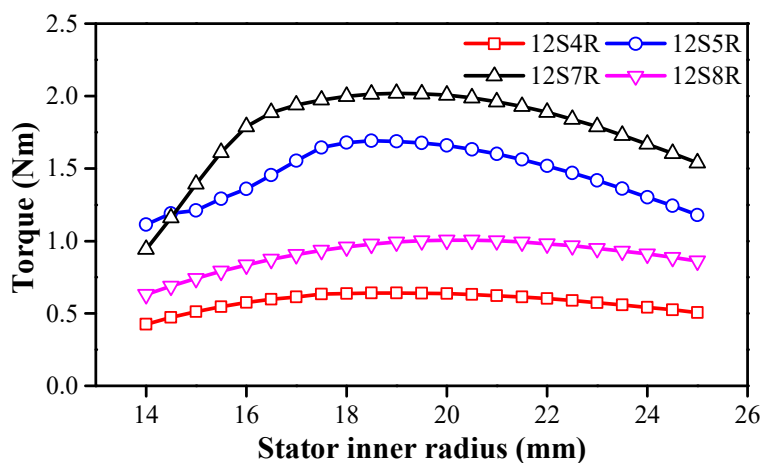


Figure 8. Influence of stator inner radius on average torque when $P_{cu_eff} = 20$ W.

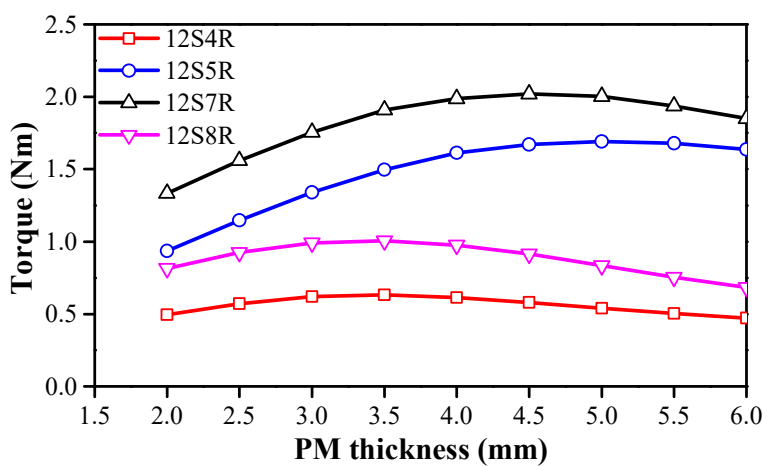


Figure 9. Influence of PM thickness on average torque when $P_{cu_eff} = 20$ W.

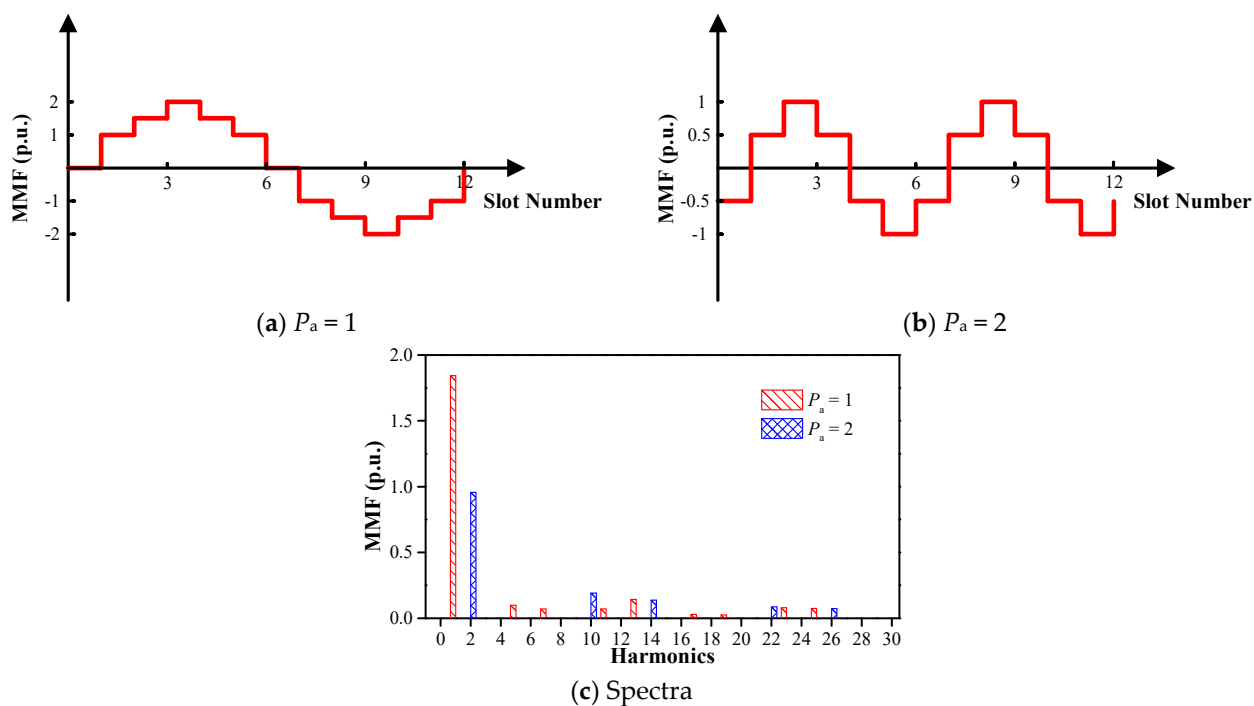


Figure 10. Armature MMFs for $P_a = 1$ and $P_a = 2$.

When the PM thickness is larger than the optimum values, the copper area and the electrical loading are reduced. Meanwhile, the reduced electrical loading also means decreased PM flux $\varphi_{PM}(F_q)$, as shown in (1).

As can be observed from Figure 11, 12S-4R/5R machines have larger values of optimum rotor tooth width than 12S-7R/8R machines. The former needs wider rotor tooth to collect more flux due to smaller rotor pole number.

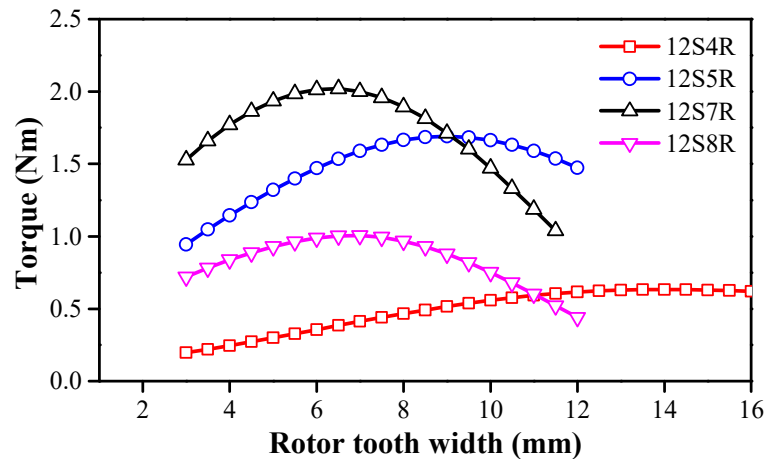


Figure 11. Influence of rotor tooth width on average torque when $P_{cu_eff} = 20$ W.

Figure 12 compares the torque waveforms of 12S machines with different rotor pole numbers. The corresponding geometric parameters are listed in Table 2. 12S-5R/7R machines deliver higher torque than 12S-4R/8R machines. In addition, the torque ripples of 12R-5R/7R machines are much lower than those of 12S-4R/8R machines, due to larger numbers of least common multiple of stator-slot number and rotor-pole number.

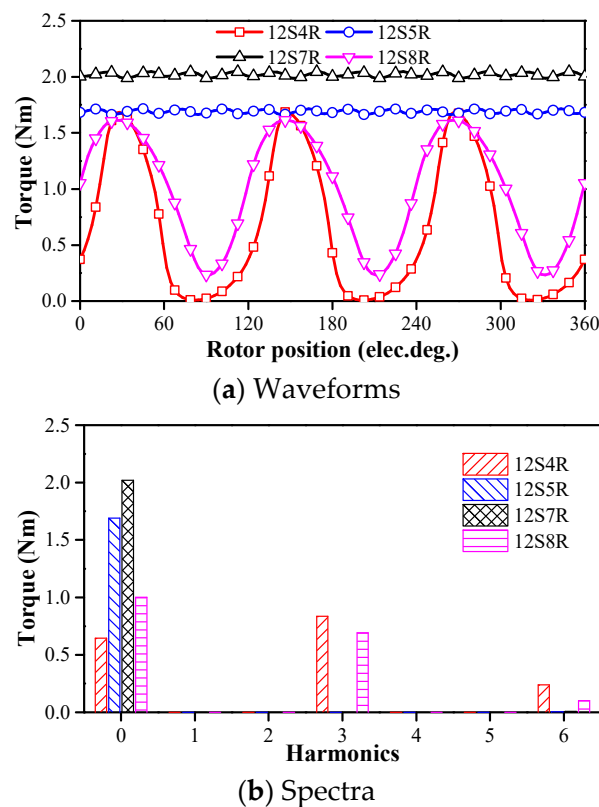


Figure 12. Comparison of torques of 12S-4R/5R/7R/8R machines when $P_{cu_eff} = 20$ W.

4. Comparison of Stator-Slot PM Machines with Tooth-Coil and Full-Pitched Windings

In this section, the 12S7R machine with FPW is compared with 12S10R with TCW, based on globally optimized topologies.

Figure 13 shows the cross sections of compared stator slot PM machines. M1 (12S7R with FPW) and M2 (12S10R with TCW) are globally optimized. M3 (12S10R with TCW) is optimized under the same PM volume as M1. The parameters are listed in Table 2.

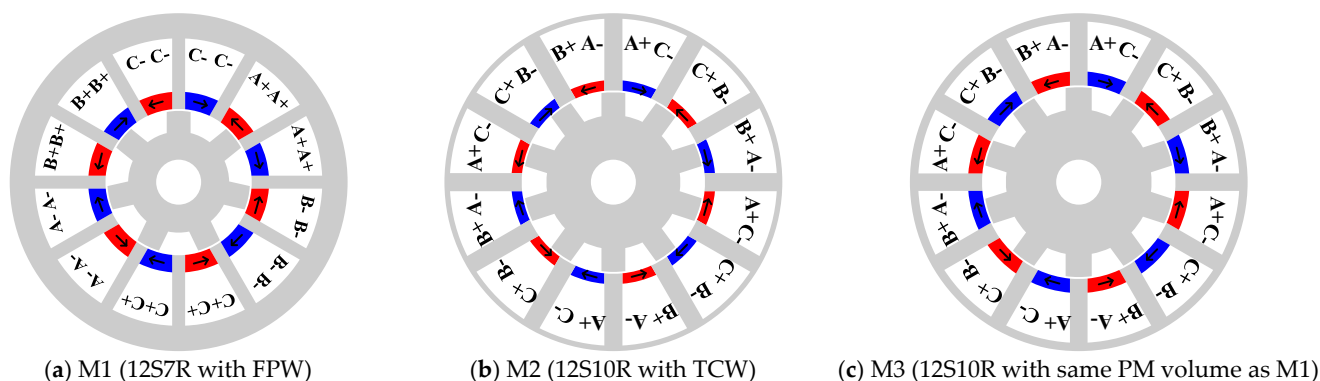


Figure 13. Cross sections of stator-slot PM machines.

On open circuit, Figure 14a–c, the PM flux linkage only circulates within the stator, if neglecting magnetic saturation. However, there is some “leakage” flux linking the stator and the rotor due to nonlinear BH characteristics of the iron core laminations. Hence, negligible back EMFs and cogging torques can be expected.

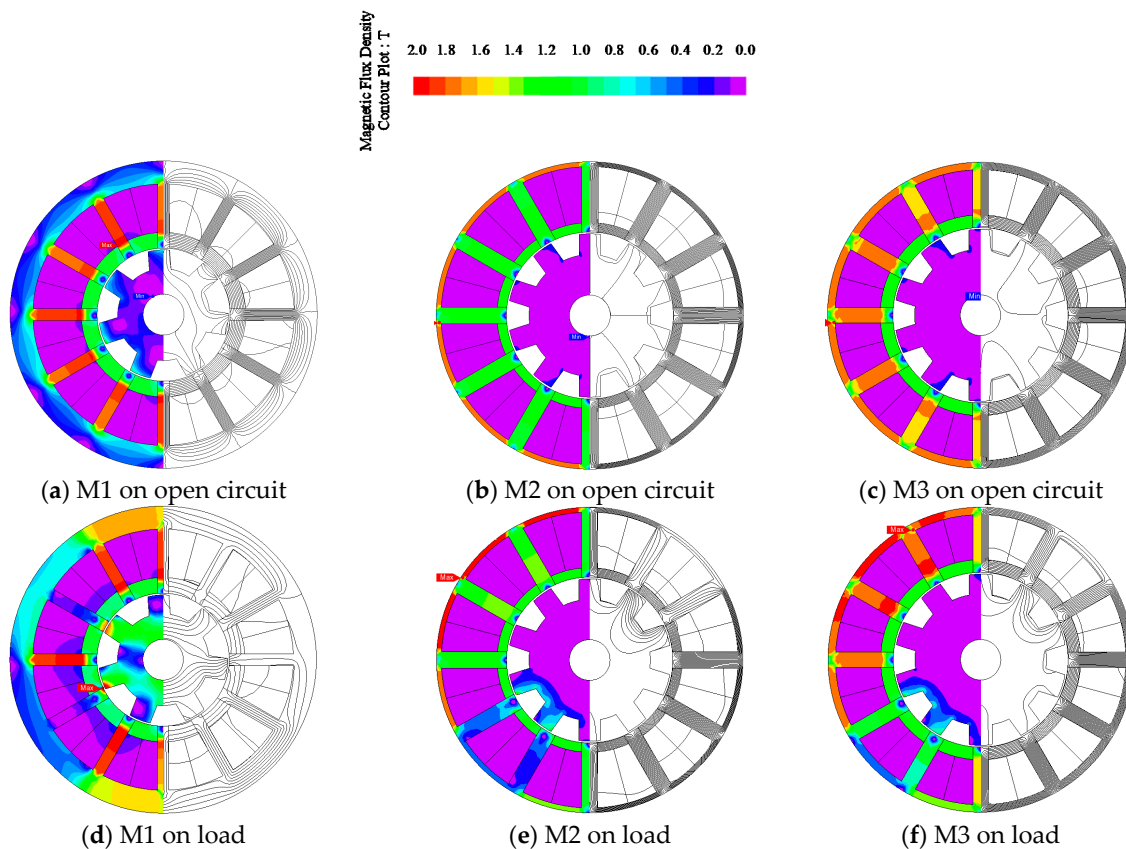


Figure 14. Flux density distributions on open circuit and load ($I_d = 0$ and $I_q = 14.14$ A).

On load, Figure 14d–f, the PM flux is forced into the airgap and the rotor side by the armature MMF, and the PM flux has improved saturation in the flux path, i.e., the stator tooth of M1 and the stator yoke of M2. This also explains the small stator yoke width in M2. Although more space is used to accommodate the copper wire, the stator yoke is not saturated on load.

By comparing Figure 14e,f, it can be observed that the on-load flux density in the stator teeth increases when increasing the PM volume. This is due to the fact that the armature MMF F_q can only force PM flux $\varphi_{PM}(F_q)$ into the airgap, and excess PM flux makes the flux path more saturated. Aside from that, the stator slot area is reduced, and so is the armature MMF F_q . Therefore, M3 generates lower torque than M2, as shown in Figure 15.

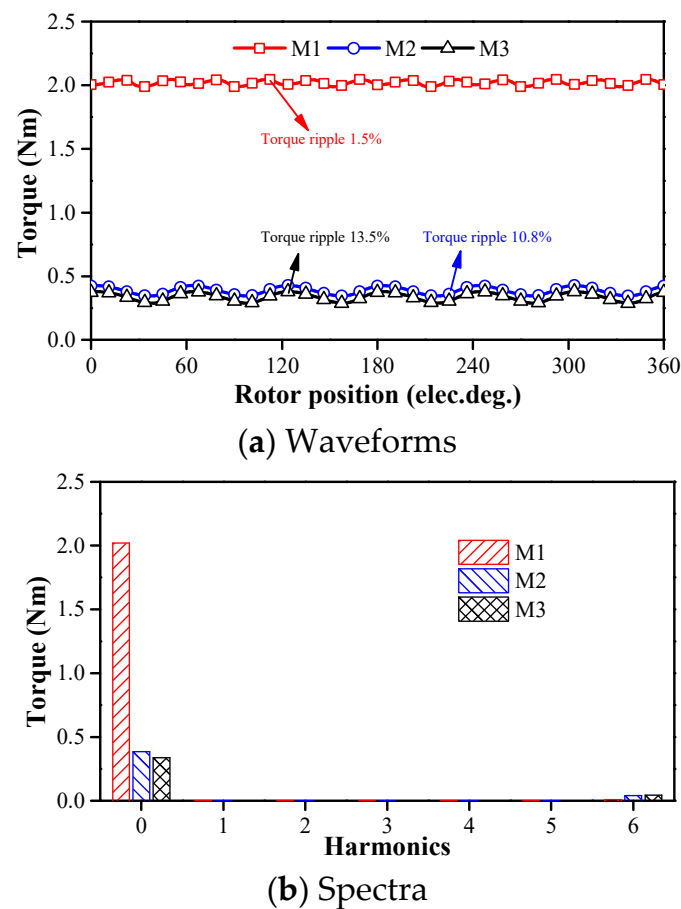


Figure 15. Comparison of torques when $I_d = 0$ and $I_q = 14.14$ A.

Figure 15 compares the torques of the three machines. As can be observed, M1 delivers the highest torque, together with the lowest torque ripple. On load, the slot/pole number combination plays an important role in affecting the torque ripple. For M1, the least common multiple LCM is 84, while that of M2 and M3 is 60, which explains the lowest torque ripple of M1. Regarding other electromagnetic performance, only M1 and M2 are compared.

In Figure 16, the airgap flux densities of the two machines are shown. M1 exhibits higher airgap flux density than M2, due to the thicker PMs resulting in more “leakage” flux, which can also be observed in Figure 14.

Similarly, the tendency of the back EMFs of the two machines can be explained. As shown in Figure 17, M1 has higher back EMF than M2.

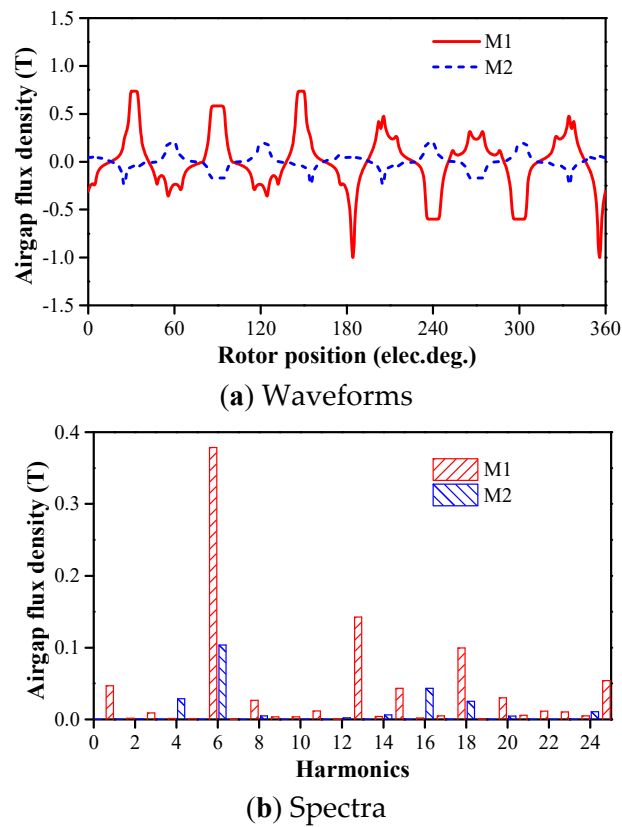


Figure 16. Airgap flux densities on open circuit.

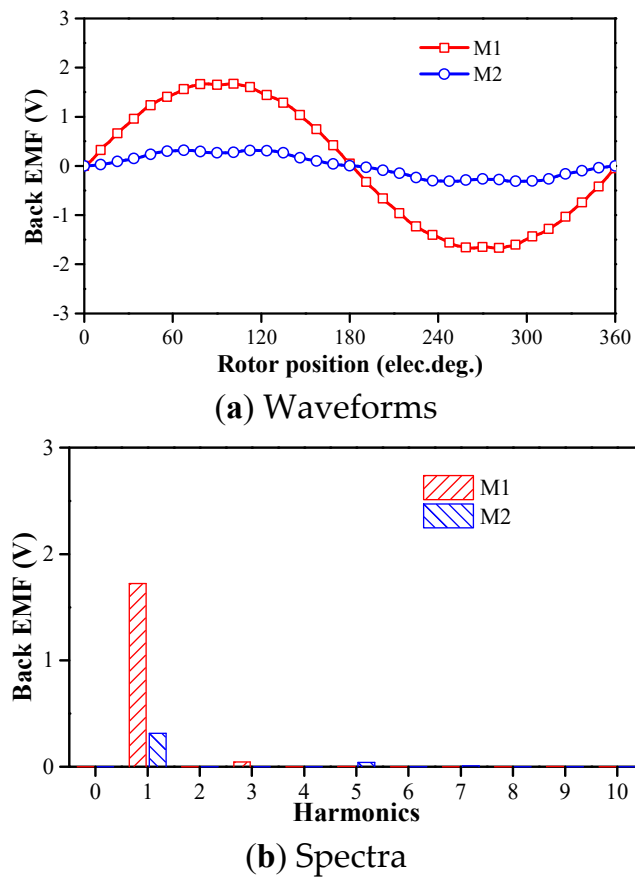


Figure 17. Back EMFs on open circuit at 600 rpm.

Cogging torque is mainly affected by the slot/pole number combination and the strength of airgap magnetic field, i.e., the amount of “leakage” flux. M1 exhibits higher cogging torque than M2 due to higher “leakage” flux, as shown in Figure 18.

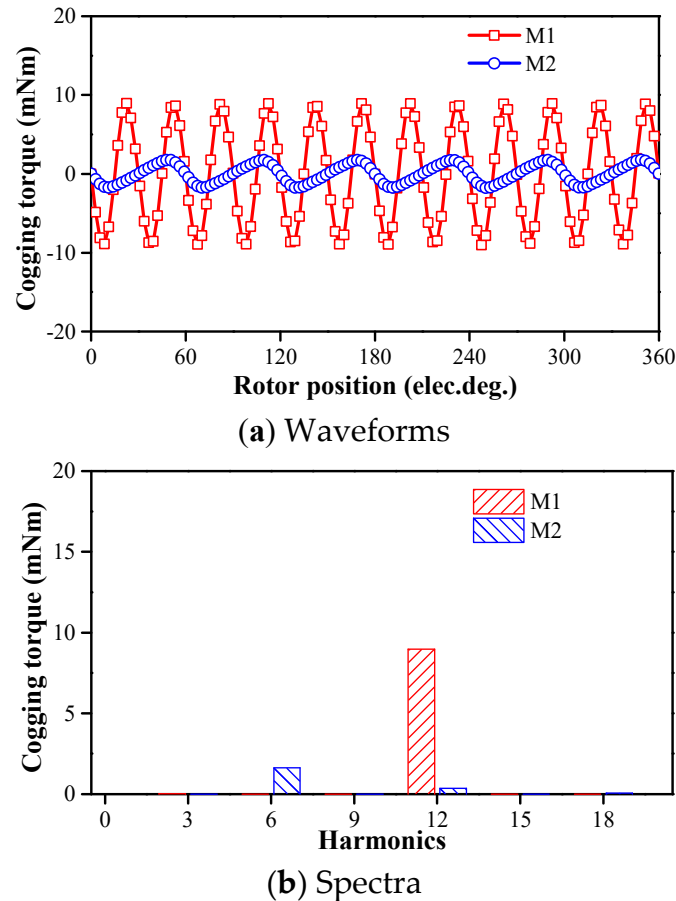


Figure 18. Cogging torques on open circuit.

The least common multiple (LCM) between the stator-slot number and the rotor-pole number of M1 and M2 is 84 and 60, respectively. Therefore, the dominant cogging torque harmonics in one electrical period are 12th and 6th, respectively, as shown in Figure 18b.

Figure 19 shows that both the machines rely on PM torque, and they have negligible reluctance torque. Figure 20 compares the torques versus armature current under $I_d = 0$ control. It should be noted that the SSCMPMMs have antisaturation capability. This antisaturation capability is due to the fact that most of the PM flux circulates within the stator core on open circuit, and the armature MMF forces the PM flux into the airgap and the rotor side at load condition. The magnetic flux path firstly becomes less saturated when the armature current increases. Then, the PM MMF and the armature MMF reach a balance, at which point the main flux path is least saturated. Afterward, the flux path becomes more and more saturated if the armature current is further increased. This phenomenon is indicated by the inductance variation versus armature current, as shown in Figure 21. The inductance variations also indicate that M2 has better overload capability.

Figure 22 compares the power factor of the two machines. M2 exhibits the slightly higher power factor on rated load, due to the smaller inductance. Although M1 has much larger inductance, its electrical frequency is lower.

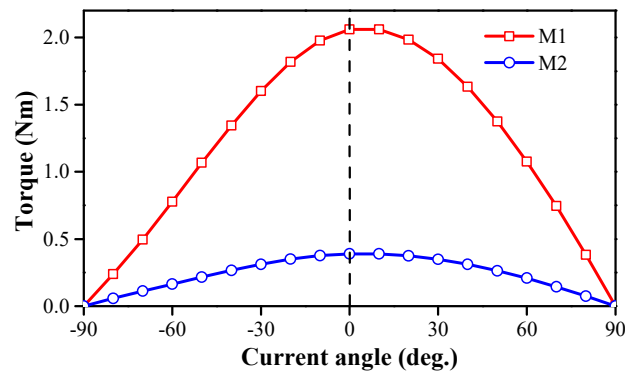


Figure 19. Torques versus current angle when the current amplitude is 14.14 A.

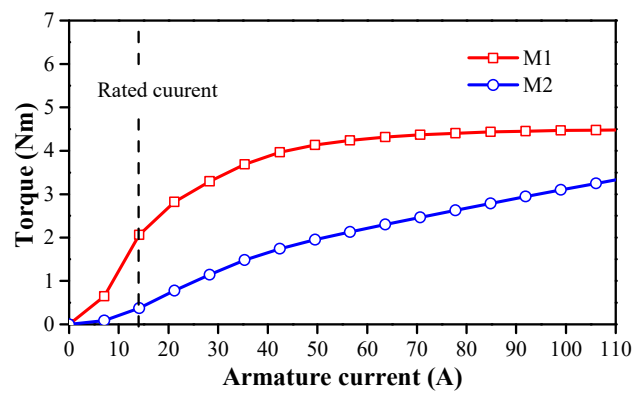
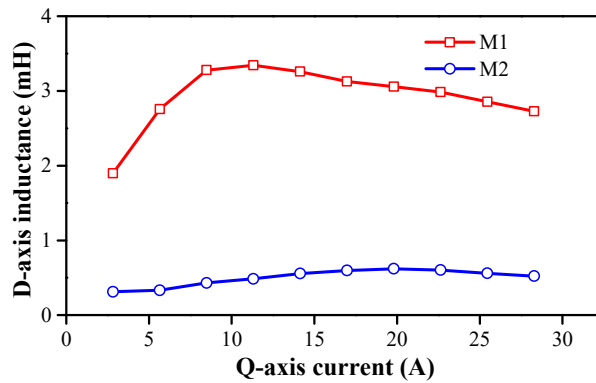
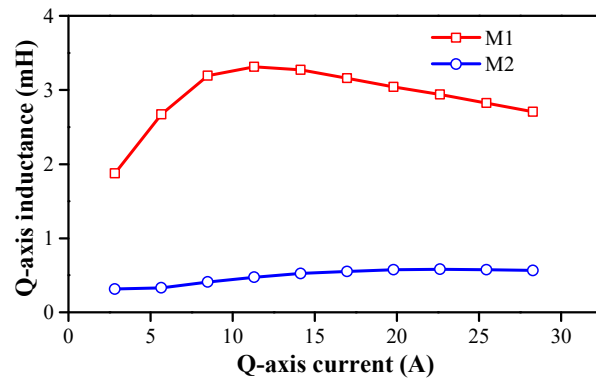


Figure 20. Torques versus armature current when $I_d = 0$.



(a) D-axis inductance



(b) Q-axis inductance

Figure 21. Inductances versus armature current when $I_d = 0$.

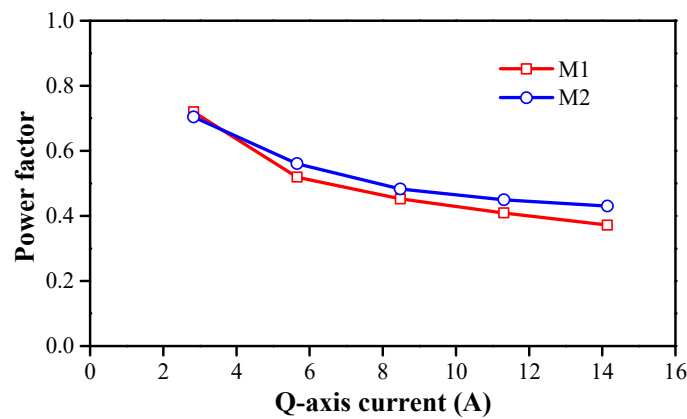


Figure 22. Power factors versus armature current when $I_d = 0$.

Figure 23 shows that the efficiencies rise with the increase of speed before reaching their maximum values, due to the increase of output power. M1 always exhibits higher efficiency than M2, albeit with much longer end-windings. The total copper losses including end-windings of M1 and M2 are 43.2 and 143.2 W, respectively.

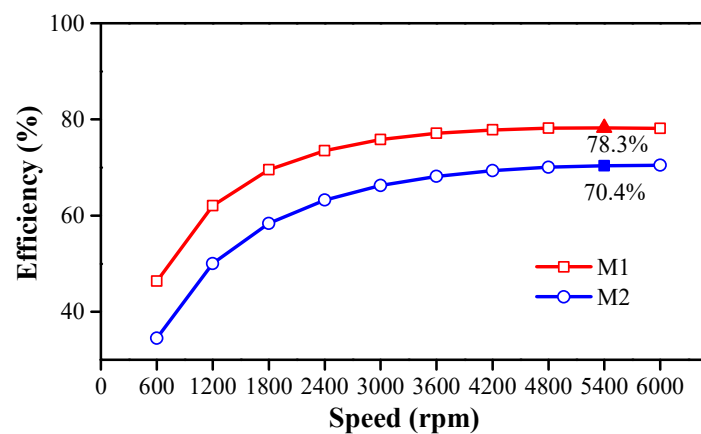


Figure 23. Efficiencies versus speed when $I_d = 0$ and $I_q = 14.14$ A.

Figure 24 compares the iron losses and PM losses. Because of the lower airgap flux density on load, as shown in Figure 25, M2 always shows lower iron loss, lower PM loss, and, interestingly, lower efficiency due to lower torque.

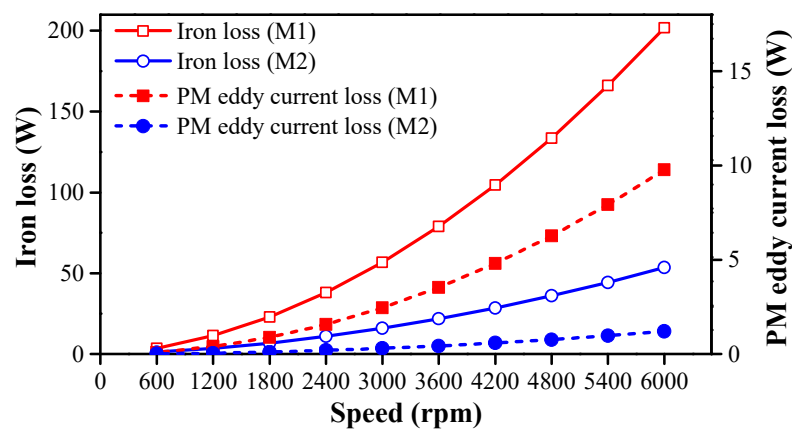


Figure 24. Iron loss and PM loss versus speed when $I_d = 0$ and $I_q = 14.14$ A.

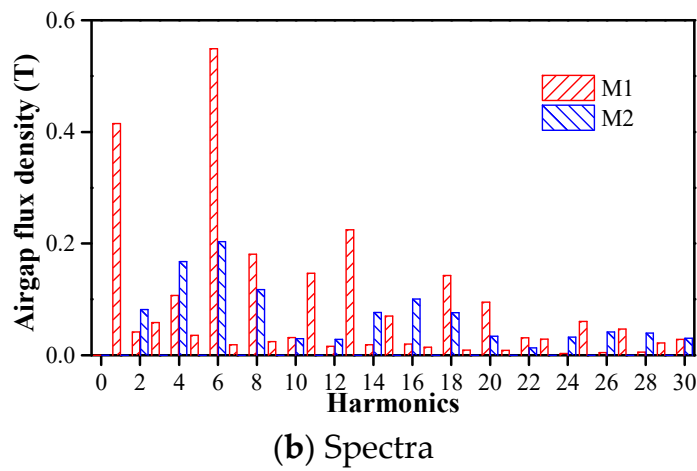
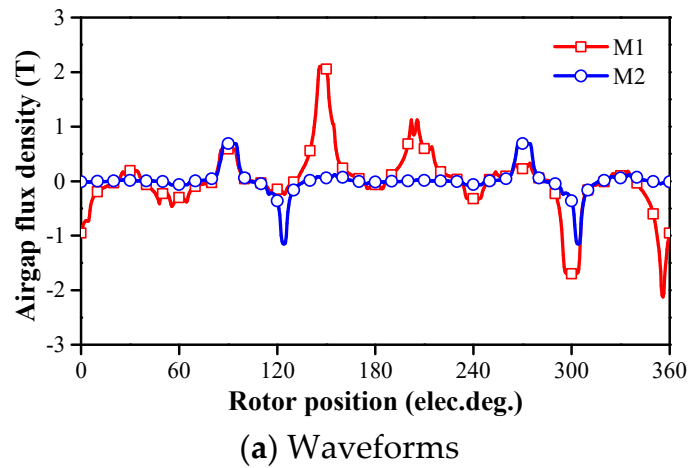


Figure 25. Airgap flux densities when $I_d = 0$ and $I_q = 14.14$ A.

Figure 26 compares the torques versus machine length. The machine length is $l_s + h_{end}$. h_{end} is the height of end-winding. The volume of the end-winding V_{end} and the volume of the effective winding V_{eff} satisfy (10).

$$V_{end} / V_{eff} = l_{end} / l_s \tag{10}$$

$$V_{end} = \pi(r_b^2 - r_t^2)h_{end} \tag{11}$$

$$V_{eff} = S_{slot}l_s \tag{12}$$

where r_b is the radius of slot bottom, r_t is the radius of slot top, and S_{slot} is the total slot area.

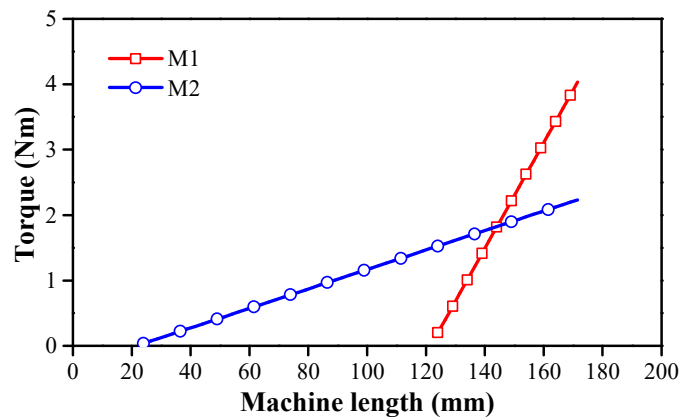


Figure 26. Torques versus machine length when $I_d = 0$ and $I_q = 14.14$ A.

As can be observed, when the machine length is smaller than 145 mm, M1 delivers lower torque than M2. However, when the machine length is larger than 145 mm, M1 is more advantageous in producing high torque. Similar efficiency tendency can be observed in Figure 27. M1 is more efficient when the machine length is over 140 mm.

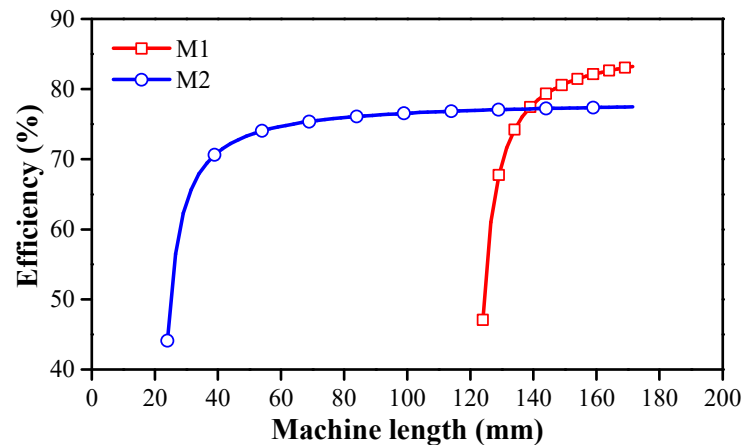


Figure 27. Efficiencies versus machine length when $I_d = 0$ and $I_q = 14.14$ A at 6000 rpm.

5. Experiment Validation

The 12S7R SSCMPMM with $y = 3$ is prototyped, as shown in Figure 28. The magnets are inserted into the stator slot after winding the stator. Due to the employment of parallel teeth, the magnets can be stuck in the stator slots. Such practice may be not applicable to mass production. The geometric parameters of the prototype are listed in Table 3.

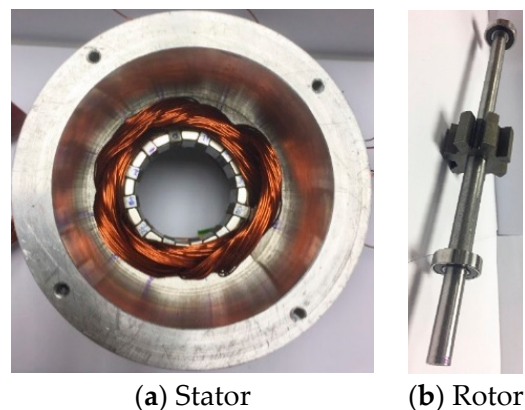
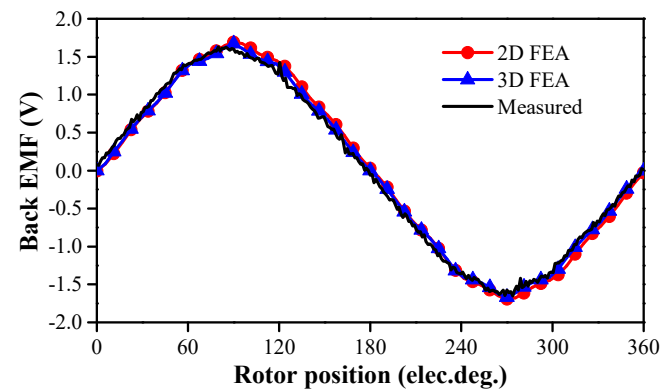


Figure 28. 12S7R prototype machine.

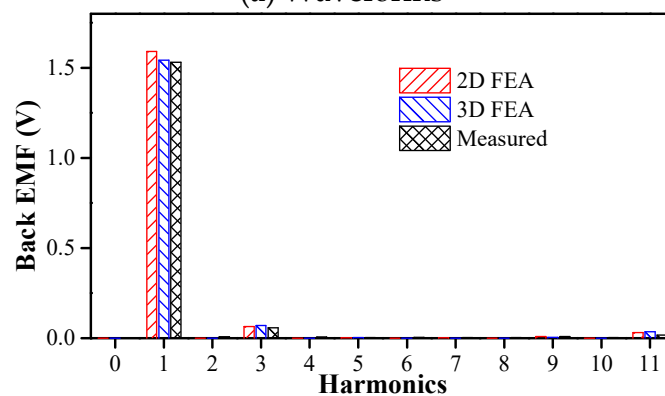
Table 3. Parameters of Prototype.

Symbol	12S7R with $y = 3$
Stator outer radius (mm)	45
Stack length (mm)	25
Airgap length (mm)	0.5
Winding pole pair number	1
Coil pitch (slot pitch)	3
N_{ph}	120
PM thickness (mm)	4.8
Stator inner radius (mm)	23
Stator tooth width (mm)	4.8
Stator yoke width (mm)	7
Rotor tooth width (mm)	7.8
Rotor slot depth (mm)	7.5

Although the open-circuit performance is produced by the “leakage” flux, and easily affected by magnetic saturation and material imperfections, it is still worth checking the back EMF. Figure 29 compares the 2D/3D FEA calculated and measured back EMFs, from which we can observe that 2D/3D FEA calculated values are close to the measured ones.



(a) Waveforms



(b) Spectra

Figure 29. FEA calculated and measured back EMFs at 600 rpm.

The static torque versus rotor position is measured by injecting dc current ($I_a = -2I_b = -2I_c = 10$ A) into the three phase windings [22]. The FEA calculated and measured static torques are shown in Figure 30. The measured static torque is around 23.6% and 18% lower than the 2D and 3D FEA calculated values. Similarly, larger difference can be observed between 2D FEA calculated and measured torque versus current curves, as shown in Figure 31.

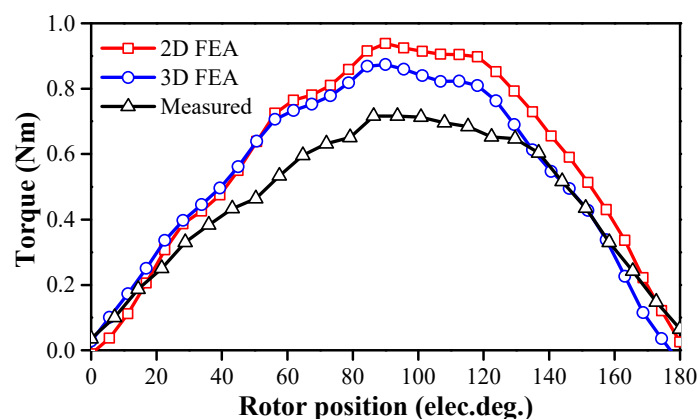


Figure 30. FEA calculated and measured static torques when $I_a = -2I_b = -2I_c = 10$ A.

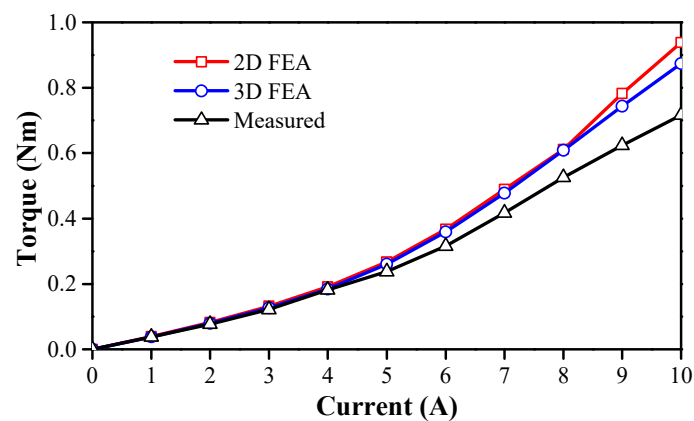


Figure 31. FEA calculated and measured torques versus current.

6. Conclusions

In this paper, stator slot circumferentially magnetized PM machines (SSCMPMMs) with full-pitched windings (FPW) are analysed. The influence of key geometric parameters is investigated for the 12 stator-slots and 4/5/7/8 rotor-poles SSCMPMMs. The 12 stator-slots 7 rotor-poles (12S7R) and 12S5R machines need larger stator yoke width and thicker PMs. The 7 poles rotor can produce the highest torque and the lowest torque ripple.

Compared with 12S10R SSCMPMM with tooth-coil windings (TCW), the 12S7R machine with FPW can deliver around 5.5 times higher torque. Meanwhile, if the total machine length is over around 140 mm, the 12S7R machine can produce higher torque density and higher efficiency compared with its 12S10R counterpart.

Author Contributions: Writing—original draft preparation, H.Q. and H.Y.; writing—review and editing, Z.Q.Z.; supervision, Z.Q.Z. All authors have read and agreed to the published version of the manuscript.

Funding: This research received no external funding.

Conflicts of Interest: The authors declare no conflict of interest.

References

- Zhang, Z.; Tao, Y.; Yan, Y. Investigation of a new topology of hybrid excitation doubly salient brushless DC generator. *IEEE Trans. Ind. Electron.* **2012**, *59*, 2550–2556. [\[CrossRef\]](#)
- Cheng, M.; Chau, K.T.; Chan, C.C. Static characteristics of a new doubly salient permanent magnet motor. *IEEE Trans. Energy Convers.* **2001**, *16*, 20–25. [\[CrossRef\]](#)
- Chau, K.T.; Sun, Q.; Fan, Y.; Cheng, M. Torque ripple minimization of doubly salient permanent-magnet motors. *IEEE Trans. Energy Convers.* **2005**, *20*, 352–358. [\[CrossRef\]](#)
- Chen, J.T.; Zhu, Z.Q. Winding configurations and optimal stator and rotor pole combination of flux-switching PM brushless AC machines. *IEEE Trans. Energy Convers.* **2010**, *25*, 293–302. [\[CrossRef\]](#)
- Hua, W.; Cheng, M.; Zhu, Z.Q.; Howe, D. Analysis and optimization of back EMF waveform of a flux-switching permanent magnet motor. *IEEE Trans. Energy Convers.* **2008**, *23*, 727–733. [\[CrossRef\]](#)
- Chen, J.T.; Zhu, Z.Q.; Iwasaki, S.; Deodhar, R. A novel E-core flux-switching PM brushless AC machine. In Proceedings of the 2010 IEEE Energy Conversion Congress and Exposition, Atlanta, GA, USA, 12–16 September 2010; pp. 3811–3818.
- Shao, L.; Hua, W.; Zhu, Z.Q.; Zhu, X.; Cheng, M.; Wu, Z. A novel flux-switching permanent magnet machine with overlapping windings. *IEEE Trans. Energy Convers.* **2017**, *32*, 172–183. [\[CrossRef\]](#)
- More, D.S.; Fernandes, B.G. Analysis of flux-reversal machine based on fictitious electrical gear. *IEEE Trans. Energy Convers.* **2010**, *25*, 940–947. [\[CrossRef\]](#)
- Gao, Y.; Qu, R.; Li, D.; Li, J.; Wu, L. Design of three-phase flux-reversal machines with fractional-slot windings. *IEEE Trans. Ind. Appl.* **2016**, *52*, 2856–2864. [\[CrossRef\]](#)
- Kim, T.H.; Lee, J. A study of the design for the flux reversal machine. *IEEE Trans. Magn.* **2004**, *40*, 2053–2055. [\[CrossRef\]](#)
- Deodhar, R.P.; Andersson, S.; Boldea, I.; Miller, T.J.E. The flux-reversal machine: A new brushless doubly-salient permanent-magnet machine. *IEEE Trans. Ind. Appl.* **1997**, *33*, 925–934. [\[CrossRef\]](#)
- Wang, C.; Nasar, S.A.; Boldea, I. Three-phase flux reversal machine (FRM). *IEE Proc. Electric Power Appl.* **1999**, *146*, 139–146. [\[CrossRef\]](#)

13. Wang, C.X.; Boldea, I.; Nasar, S.A. Characterization of three phase flux reversal machine as an automotive generator. *IEEE Trans. Energy Convers.* **2001**, *16*, 74–80. [[CrossRef](#)]
14. Afinowi, I.A.A.; Zhu, Z.Q.; Guan, Y.; Mipo, J.; Farah, P. A novel brushless AC doubly salient stator slot permanent magnet machine. *IEEE Trans. Energy Convers.* **2016**, *31*, 283–292. [[CrossRef](#)]
15. Xie, K.; Li, D.; Qu, R.; Yu, Z.; Gao, Y.; Pan, Y. Analysis of a flux reversal machine with quasi-Halbach magnets in stator slot opening. *IEEE Trans. Ind. Appl.* **2019**, *55*, 1250–1260. [[CrossRef](#)]
16. Li, H.; Zhu, Z.Q. Influence of adjacent teeth magnet polarities on the performance of flux reversal permanent magnet machine. *IEEE Trans. Ind. Appl.* **2019**, *55*, 354–365. [[CrossRef](#)]
17. Gao, Y.; Qu, R.; Li, D.; Li, J.; Zhou, G. Consequent-pole flux-reversal permanent-magnet machine for electric vehicle propulsion. *IEEE Trans. Appl. Supercond.* **2016**, *26*. [[CrossRef](#)]
18. Zhu, Z.Q.; Pothi, N.; Xu, P.L.; Ren, Y. Uncontrolled generator fault protection of novel hybrid-excited doubly salient synchronous machines with field excitation current control. *IEEE Trans. Ind. Appl.* **2016**, *55*, 3598–3606. [[CrossRef](#)]
19. Du, Y.; Xiao, F.; Hua, W.; Zhu, X.; Cheng, M.; Quan, L.; Chau, K.T. Comparison of flux-switching PM motors with different winding configurations using magnetic gearing principle. *IEEE Trans. Magn.* **2016**, *52*. [[CrossRef](#)]
20. More, D.S.; Fernandes, B.G. Power density improvement of three phase flux reversal machine with distributed winding. *IET Electr. Power Appl.* **2010**, *4*, 109–120. [[CrossRef](#)]
21. Li, D.; Qu, R.; Li, J.; Xu, W.; Wu, L. Synthesis of switched flux permanent magnet machines. *IEEE Trans. Energy Convers.* **2016**, *31*, 106–117. [[CrossRef](#)]
22. Zhu, Z.Q. A simple method for measuring cogging torque in permanent magnet machines. In Proceedings of the 2009 IEEE Power & Energy Society General Meeting, Calgary, AB, Canada, 26–30 July 2009. [[CrossRef](#)]